Available online at www.sciencedirect.com

ScienceDirect

ELSEVIER

International Journal of Mass Spectrometry 269 (2008) 1–11

International Journal of Mass Spectrometry

www.elsevier.com/locate/ijms

Review

Spectroscopy and chemical dynamics of group II metal ion-formaldehyde complexes

Paul D. Kleiber*, Wenyun Lu[1], Yohannes Abate[2]

Department of Physics and Astronomy, University of Iowa, Iowa City, IA 52242, United States

Received 30 July 2007; received in revised form 7 September 2007; accepted 10 September 2007
Available online 14 September 2007

Abstract

This review focuses on the spectroscopy and chemical dynamics of bimolecular complexes of group II metal ions with formaldehyde using mass resolved photodissociation spectroscopy techniques. Photodissociation spectroscopy of isolated metal ion-molecule complexes gives quantitative information about the structure and bonding of the complex, and valuable insight into the electronic nonadiabatic interactions that determine the reaction pathways and energy partitioning. The experimental techniques of photodissociation spectroscopy are briefly reviewed. Results from several experiments are then discussed including the photodissociation of Mg^+-, Ca^+-, and Zn^+-based complexes with formaldehyde. Despite the similarities in valence electronic structure for these metal ions, the spectroscopy and quenching dynamics show remarkable differences. We also compare results with the photodissociation spectroscopy of Mg^+-acetaldehyde where additional chemical reaction channels are accessible.
© 2007 Elsevier B.V. Published by All rights reserved.

Keywords: Photodissociation; Spectroscopy; Formaldehyde; Acetaldehyde; Cluster

Contents

---

* Corresponding author. Tel.: +1 319 335 1841; fax: +1 319 335 1753.
E-mail address: pkleiber@uiowa.edu (P.D. Kleiber).
[1] Present address: Lewis-Sigler Institute for Integrative Genomics, Princeton University, Princeton, NJ 08544, United States.
[2] Present address: Department of Chemistry, University of California, Berkeley, CA 94720-1460, United States.

1387-3806/$ – see front matter © 2007 Elsevier B.V. Published by All rights reserved.
doi:10.1016/j.ijms.2007.09.002

1. Introduction

The coupling of supersonic molecular beam sources and time-of-flight mass spectrometry with laser spectroscopic techniques allows experimenters to investigate bonding interactions and chemical dynamics in a variety of weakly bound molecular clusters through photodissociation spectroscopy [1–9]. The photodissociation of a weakly bound bimolecular complex serves to mimic a bimolecular "half-collision" process, offering an effective experimental approach to the study of excited state molecular dynamics [9]. In many cases the structure of the precursor complex can be determined through a combination of ab initio calculations and bound state spectroscopy. Following laser excitation the subsequent excited state half-collision begins with a well-characterized geometry, electronic orbital alignment, energy, and angular momentum. The photofragment action spectra yield information about the structure and lifetime of the complex, and the dynamical effects that determine the energy partitioning and microscopic branching in multichannel reactions. Such experiments give insight into the nuclear motion dynamics, stereochemical effects, and the electronic nonadiabatic interactions that couple the Born–Oppenheimer potential energy surfaces [9].

The primary aim of our work has been to investigate C–H, C–C, and C–O bond activation processes by light metal atoms in reactions with small organic molecules, such as alkane and alkene hydrocarbons and organic derivatives including aldehydes and carboxylic acids [9–22]. This review focuses on the photodissociation spectroscopy of weakly bound bimolecular complexes of group II metal ions with formaldehyde [17–21]. Singly charged group IIa and IIb metal ion based complexes are ideally suited for such experiments because they support strong metal-centered transitions that are easily accessed in the visible and near UV. In addition, owing to their open shell "radical" structure, nonadiabatic interactions will be especially important and chemical-quenching pathways will often be open.

The activation of C–H, C–C, and C–O bonds of carbonyls by metal atoms and ions are among the most important processes in chemistry [23–25]. Simple organic carbonyls are vital elements in chemical synthesis and many reactions in synthetic organic chemistry or enzyme-catalyzed transformations rely on metal, metal salt, or metal containing compounds as catalysts. The photodissociation spectroscopy of isolated metal ion-carbonyl clusters can give insight into the bonding interactions and dynamical effects that lie at the core of such processes. The main focus here will be on one of the simplest carbonyls, formaldehyde. The chemistry of formaldehyde is of interest, both for fundamental scientific reasons and because of its importance in chemical synthesis and many naturally occurring processes in combustion, atmospheric chemistry, and astrochemistry [23–27].

Gas phase radical reactions with formaldehyde are generally thought to proceed through one of two competing mechanisms, direct H-atom abstraction or an addition reaction involving attack on the CO π-bond, followed by C–H bond insertion and decomposition, e.g.,

$$\mathrm{X + CH_2O \rightarrow [XHCHO] \rightarrow XH + CHO} \tag{1}$$

$$\mathrm{X + CH_2O \rightarrow [H_2COX] \rightarrow [HXCHO] \rightarrow XH + CHO} \tag{2}$$

Experimental and theoretical studies of the $O(^3P) + CH_2O$ and $OH + CH_2O$ reactions have concluded that the H-atom abstraction mechanism dominates, at least at low energies [28–30]. For $H + CH_2O$ reactions, experiments suggest that abstraction and addition-elimination pathways may be competitive [31]. In transition metal reactions with formaldehyde, however, it is often found that reaction proceeds through a multistep insertion process [32,33], e.g.,

$$\mathrm{M + CH_2O \rightarrow H_2COM \rightarrow HMCHO \rightarrow H_2MCO \rightarrow MH_2 + CO} \tag{3a}$$

or

$$\mathrm{M + CH_2O \rightarrow H_2COM \rightarrow HMCHO \rightarrow H_2MCO \rightarrow H_2 + MCO} \tag{3b}$$

Studies of the chemical interactions of group II metal ions with CH_2O are particularly interesting because, as with H-atoms, multiple reaction pathways might be open.

While the primary focus will be on metal ion-formaldehyde complexes, selected results from the photodissociation spectroscopy of metal-ion acetaldehyde clusters will also be briefly discussed. Acetaldehyde offers an interesting comparison since the chemistry allows for studying the competition between C–H and C–C bond breaking processes in the isolated complex. Reactions of acetaldehyde with transition metals and transition metal ions have been studied experimentally using crossed beam experimental methods and in theoretical calculations [34–36]. While the C–H and C–C bonds are of similar strength, steric effects might be expected to favor C–H bond activation because of repulsion from the H-atoms in the methyl group. Indeed, one of the intriguing results from studies of neutral transition metal chemistry involving small alkane hydrocarbons is that the thermal chemistry is often dominated by initial C–H (rather than C–C) bond activation, even though the alkane C–C bonds may be weaker than the C–H bonds [37]. The reasons for this preference in neutral transition metal reactions are not completely understood [38]. Steric hindrance effects may play an important role. Theory also suggests that the directional nature of the sp^3-hybridized orbitals on alkane carbon atoms may be important, making it difficult to reorient the orbital into the required transition state geometry, thereby raising the activation barrier for C–C bond insertion [39]. In acetaldehyde the sp^2-bonding of the carbonyl carbon, could allow for easier reorientation of the orbitals and more effective activation of the C–C bond than in alkane hydrocarbons.

2. Experimental methods

The experimental apparatus for our photodissociation spectroscopy work is typical [9,40], consisting of a Smalley-type laser vaporization cluster source [41] coupled to an angular reflectron time-of-flight mass spectrometer (RTOFMS) (R.M. Jordan Co.). Cluster ions from the source are mass-selected and probed with a tunable UV–vis pulsed laser system in the turning point region of the reflectron. The daughter ions are mass analyzed in the second leg of the RTOFMS and detected with a multichannel plate detector in a standard tandem time-of-flight arrangement. Tandem mass-spectrometry affords the ability to uniquely mass identify and select the parent complex from the molecular beam source, which is critical when there is limited spectral structure in the photodissociation spectrum, as will often be the case in systems that are rapidly quenched. Signals are collected with a gated integrator, digital storage scope, or multichannel scaler, depending on the signal level.

Metal ion based clusters are generated by laser ablation of a metal rod using the second harmonic of a pulsed Nd:YAG laser (Spectra Physics, DCR 11). The sample rod is fixed to the face of a pulsed supersonic valve (R.M. Jordan Co., PSV) and positioned directly in the free jet expansion from the PSV nozzle. The sample rod is connected to a drive mechanism allowing for rotation and translation of the rod to keep the metal sample surface fresh. The ablation laser pulse is timed to overlap the gas pulse from the PSV, and adjusted to optimize formation of the desired cluster. The ablation laser pulse intensity is kept low to minimize overheating of the laser produced plasma and optimize the formation of weakly bound bimolecular complexes with low internal temperatures. Too large a laser fluence results in warmer clusters, greater fragmentation and more “prereaction” in the source region.

The PSV is typically operated at a backing pressure of ∼40 psi, seeded with a 1–10% mix of sample in a carrier gas. For the formaldehyde clusters, solid paraformaldehyde is heated to produce the vapor, which is then combined with Ar carrier gas in a mixing cylinder [17]. Ion-molecule clusters form in the supersonic expansion of the metal vapor plasma with a seeded carrier gas flow. The gas expansion passes through a conical skimmer into the differentially pumped extraction chamber. Cluster ions are pulse extracted at right angles and accelerated into the third differentially pumped chamber, the flight tube of the RTOFMS. The extraction and acceleration voltages are adjusted for Wiley–McLaren focusing [42], and the typical beam energy is 1.4 keV. The ion packets are transversely focused with a three element Einzel lens, and pass through a pulsed mass gate for preliminary mass selection.

A Nd:YAG pumped OPO (Spectra Physics, PRO-250/MOPO SL) is time delayed to excite the “target” parent ion at the turning point inside the reflectron. The OPO covers the visible (430–690 nm) and near IR (730–1800 nm) with a bandwidth of $<0.2\,\mathrm{cm}^{-1}$. The near-UV region (215–419 nm) is reached by nonlinear frequency mixing (Spectra Physics, WEX). In this arrangement signal fluctuations due to timing jitter are minimized since the residence time near the turning point is long. In addition, accurate branching ratio measurements are easily made because the unreacted parent ion and all of the daughter ions can be detected simultaneously. (This assumes that mass discrimination effects are negligible, which is usually a good approximation in our apparatus for the small clusters of interest here [40].) Following photolysis, the parent and daughter fragment ions are reaccelerated in the reflectron and focused to an off-axis microchannel plate detector (MCP). A digital oscilloscope is used to monitor the mass spectrum and is interfaced to a laboratory personal computer for further data analysis. When signals are large, a series of gated integrators can be used to measure the integrated signal in the parent and in each daughter ion packet. For small signals, a multichannel scaler can be used for single ion counting.

The mass-resolved product action spectra are determined by measuring the integrated daughter ion signal as a function of photolysis laser wavelength, normalized by the parent ion signal and probe laser intensity. Signal-to-noise is limited primarily by short term fluctuations and long term drift in the molecular beam intensity from the vaporization source. Laser power linearity tests are used to discriminate against multiphoton dissociation processes. However, in the photoexcitation of long-lived bound states of the complex, the resonance transitions are easily saturated and it is not always possible to rule out some contribution from multiphoton dissociation processes through higher lying states. While such processes can usually be safely ignored in assigning the spectra, they can complicate the interpretation of the subsequent dissociation dynamics.

3. Photodissociation spectroscopy of M^+-aldehyde complexes

3.1. Mg^+-formaldehyde

3.1.1. Electronic structure calculations

Results for Mg^+-formaldehyde form a useful basis for discussing the spectroscopy of all of the group II metal ion-aldehydes under consideration. Electronic structure calculations on the Gaussian 98 platform [43] show Mg^+-formaldehyde to be bound in a C_{2v} Mg^+–OCH_2 equilibrium geometry [17]. The bonding is predominantly electrostatic and is enhanced in part by a polarization of charge on the O atom that leads to a slight weakening of the C–O bond and opening of the H–C–H angle. Beyond these small changes the aldehyde moiety remains relatively undistorted from its isolated equilibrium geometry. For Mg^+–OCH_2, the M–O bond dissociation energy is $D_e''(\mathrm{Mg–OCH_2}) = 1.51\,\mathrm{eV}$, with an Mg^+–O equilibrium bond length of $R_{\mathrm{Mg–O}} = 1.99\,\text{Å}$, in an unrestricted Hartree–Fock UHF/6-311++g(2d,2p) level calculation [17]. Including correlation effects in a density functional theory (DFT) calculation using Becke's three parameter hybrid method with the Lee, Yang, Parr correlation functional and unrestricted wavefunctions (UB3LPY) shows that the intermolecular bond strength decreases slightly to $D_e''(\mathrm{Mg–OCH_2}) = 1.43\,\mathrm{eV}$ at the UB3LPY/6-311++g(2d,2p) level. Correlation increases the size of the interacting orbitals and lead to greater steric repulsion. Selected spectroscopic parameters are summarized in Table 1. A search of the ground state potential energy surface also finds a second stable isomer that corresponds to the HMgCHO insertion complex. This structure lies at much higher energy, 2.30 eV above the global minimum, but is energetically accessible from the excited electronic states. The UB3LYP/6-311++g(2d,2p)

Table 1
Table of selected spectroscopic constants for $M^+(CH_2O)$ complexes (experimental values in parentheses)

$M^+(CH_2O)$	Mg	Ca	Zn
$ns\sigma(A')$[a]	C_{2v} (C_{2v})	C_{2v} (C_{2v})	C_s
D_e (eV)	1.43 (1.21)	1.30 (0.9)	1.49
R_{MO} (Å)	1.99	2.28	2.09
∠(M–O–C)	180 (>165)	180 (>175)	140
ω_{MO} (a') (cm^{-1})	372	279	280
ω_{IP} (a') (cm^{-1})	75	114	151
ω_{OP} (a'') (cm^{-1})	164	158	260
$np_x\pi$ (A'')[b]	C_{2v} (C_s)	C_{2v}	C_s
T_e (eV)	3.44 (2.91)	2.52 (2.28)	4.14 (4.71)
R_{MO} (Å)	1.87	2.14	1.89
∠(M–O–C)	180	180	155
ω_{MO} (a') (cm^{-1})	480	471 (371)	399 (470)
ω_{IP} (a') (cm^{-1})	120	179	158
ω_{OP} (a'') (cm^{-1})	262	373 (242)	327 (277)
$np_y\pi$ (A')[b]	C_s (C_s)	C_s (C_s)	C_s (dissociates)
T_e (eV)	3.63 (3.70)	2.95 (2.77)	4.32 (4.83)
R_{MO} (Å)	1.95	2.46	1.95
∠(M–O–C)	144 (139)	149 (147)	138
ω_{MO} (a') (cm^{-1})	465 (462)	253 (316)	364
ω_{IP} (a') (cm^{-1})	187 (212)	140 (130)	226
ω_{OP} (a'') (cm^{-1})	258	206 (172)	393
$np_z\sigma$ (A')[b]	C_{2v}	Dissociates	Not observed
T_e (eV)	5.08 (5.02)	4.63 (4.31)	
R_{MO} (Å)	1.94		
∠(M–O–C)	180		
ω_{MO} (a') (cm^{-1})	356 (360)		
ω_{IP} (a') (cm^{-1})	47 (85)		
ω_{OP} (a'') (cm^{-1})	186 (234)		

[a] Ground state (ns) calculations at the UB3LYP/6-311++g(d,p) level.
[b] Excited state (np) calculations at the UCIS/6-311++g(d,p) level.

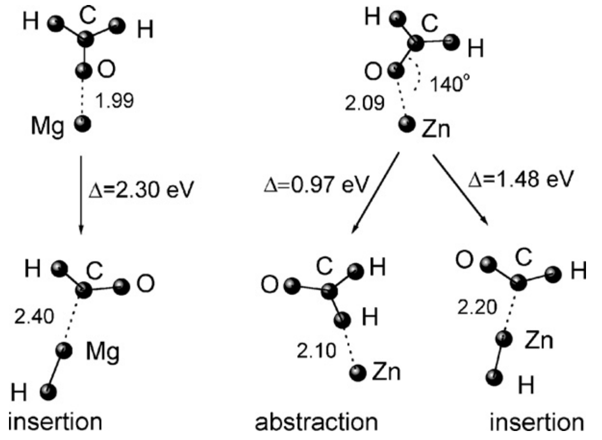

Fig. 1. Schematic diagram showing selected stationary points on the ground state potential energy surface for Mg^+– and Zn^+–CH_2O, calculated at the UB3LYP/6-311++g(d,p) level. The global minima are found in O-end-on geometry. Other stable geometries corresponding to insertion or abstraction reaction intermediates lie at higher energies but can be accessed through nonadiabatic coupling from the excited state surfaces. Results suggest that reactive quenching is dominated by an insertion process in Mg^+-formaldehyde and an abstraction process in Zn^+-formaldehyde.

optimized geometries for these stable ground state geometries are shown schematically in Fig. 1a. No stable Mg–HCHO abstraction complex was found in the calculations.

The excited state structure for the metal ion-aldehydes is complicated by a large number of interacting electronic states. Radiative transitions to low-lying doublet states with both metal-centered $p \leftarrow s$ and aldehyde-centered $\pi^* \leftarrow n$ character are possible. The metal-based transitions correlating with $Mg^+(3p \leftarrow 3s)$ resonance excitation will dominate the absorption spectrum. Simple electrostatic arguments, supported by ab initio calculations, indicate that the Mg^+-based $3p\pi$ excited states will be more attractive than the $3s\sigma$ ground state since the electron density along the intermolecular axis is reduced leading to an increase in the strength of the ion-dipole attraction. On the other hand, the $3p\sigma$ state is less strongly bound than the ground state owing to the increase in σ-repulsion along the Mg–O bond axis.

Unrestricted configuration interaction with single excitation (UCIS) calculations for the low-lying doublet excited states of $Mg^+(CH_2O)$ find three strong Mg^+-based absorption bands that correlate with the alignment of the excited Mg^+ 3p-orbital in the complex [17] at the UCIS/6-311++g(2d,2p) level. The two metal-based $3p\pi$ bands [$3p_x\pi(A'')$ and $3p_y\pi(A') \leftarrow 3s\sigma(A')$] are significantly red-shifted from the Mg^+ $3p \leftarrow 3s$ resonance line, while the third band, $3p_z\sigma(A') \leftarrow 3s(A')$, is blue-shifted, consistent with the simple electrostatic arguments above. (The initial plane of the atoms is chosen as the symmetry plane.) UCIS calculations also predict a much weaker transition in the near UV that correlates with the predominantly aldehyde-based $\pi^* \leftarrow n$ transition.

The first excited state in the complex correlates with a predominantly $Mg^+(3p_x\pi)$-based state with the metal p_x-orbital aligned perpendicular to the plane of the molecule. The optimized excited state geometry shows a considerable shortening in the Mg–O bond, consistent with the formation of a partial Mg–O π-bond in this excited state [17]. While the transition is predominantly Mg^+-centered, orbital analysis shows that the radiative transition can be more properly described as excitation from the Mg^+-based s-orbital into an orbital that has both Mg^+ p_x and CO π^* character. Selected excited state spectroscopic parameters are also given in Table 1.

The second excited state is $Mg^+(3p_y\pi)$-based, with the metal p_y-orbital lying in the molecular plane but roughly perpendicular to the Mg–O bond. UCIS/6-311++g(2d,2p) geometry optimization for this excited state shows a structural change to a bent C_s geometry [17]. The atoms remain in the molecular symmetry plane but the Mg–O–C bond angle decreases dramatically from linear in the ground state to ∠(Mg–O–C) ∼144° in the excited state. The bonding is still primarily electrostatic but the complex bends in order to minimize steric repulsion between the O nonbonding n-orbitals and the in-plane Mg^+ p_y-orbital. The large change in the Mg–O–C bond angle indicates that the intermolecular in-plane bending vibration mode will be especially strong in the absorption spectrum.

The third excited doublet state in each case correlates predominantly with the formaldehyde-based excited state that arises from an $\pi^* \leftarrow n$ excitation. We find that this formaldehyde-based absorption band in the complex is relatively unshifted

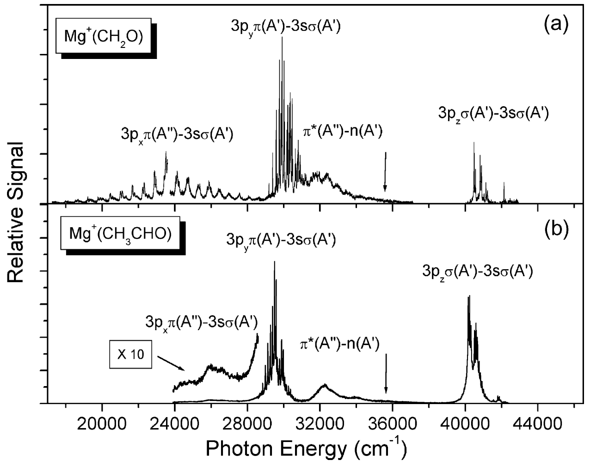

Fig. 2. Action spectra leading to Mg^+ product in the photodissociation of (a) $Mg^+(CH_2O)$ and (b) $Mg^+(CH_3CHO)$. Vertical arrows mark the energy of the Mg^+ (3p ← 3s) atomic resonance line.

from its position in the bare molecule. However, this nominally weak transition gains strength by mixing in metal p_x-orbital character.

The fourth excited state correlates to the $Mg^+(3p_z\sigma)$-based excited state with the Mg^+ p_z-orbital lying along Mg–O intermolecular axis. Calculations show a shortening of the Mg–O bond and stretching of the C–O bond, consistent with the formation of a partial Mg–O σ-bond in this state that is not expected from simple electrostatic arguments. These predictions are, however, in good agreement with the main experimental observations [17] (Table 1).

3.1.2. Electronic band spectra

The action spectrum for photodissociation to Mg^+ product from $Mg^+(CH_2O)$ is shown in Fig. 2a. Simple ligand loss to Mg^+ is the primary dissociation channel; however, reactive dissociation to MgH^+ is also observed at higher energies [17]. The Mg^+ action spectrum shows four distinct absorption bands that can be assigned to the Mg^+-based 3p–3s transitions and the aldehyde-based $\pi^* \leftarrow n$ transition as indicated by the UCIS calculations, and as given in Fig. 2a. The lowest energy band is assigned to excitation of the Mg^+-based $3p_x\pi(A'')$ state, mixed with carbonyl π* orbital character. The highly structured band in the 26,000 cm^{-1} range is assigned to excitation of the Mg^+-based $3p_y\pi(A')$ state. A weak continuum band centered near 32,000 cm^{-1} is assigned to the predominantly carbonyl based $\pi^* \leftarrow n$ transition, mixed with Mg^+ $3p_x\pi$ orbital character. The highest energy band shown in Fig. 2, centered near 40,000 cm^{-1}, is assigned to the Mg^+-based $3p_z\sigma(A') \leftarrow 3s\sigma(A')$ transition. Transition energies are in reasonably good agreement with the UCIS calculations (Table 1).

3.1.3. Rovibronic analysis

The lowest energy band $3p_x\pi(A'') \leftarrow 3s\sigma(A')$ of $Mg^+(CH_2O)$ shows extensive vibrational structure over an energy range spanning >10,000 cm^{-1}. The band contains a long series of broad vibrational resonance features. This high degree of vibrational excitation implies a large geometry change on excitation. Spectral analysis shows two overlapping vibrational progressions based on mode frequencies of ∼640 and ∼1240 cm^{-1} [17]. The excitation of multiple quanta in these high frequency vibrational modes, coupled with the large red shift of the band from the Mg^+ 3p ← 3s resonance transition indicates a strong chemical interaction in this state of the complex. As UCIS calculations show, the radiative transition is of mixed Mg^+ p_x- and formaldehyde π*-orbital character. Transferring electron density into the π*-antibonding LUMO of formaldehyde leads to a significant weakening of the C–O bond and formation of a partial Mg–O π-bond. The $\pi^* \leftarrow n$ transition in isolated formaldehyde stretches the C–O bond and causes a distortion out-of-plane to a pyramidal geometry; in the complex this results in very high intramolecular vibrational excitation of the formaldehyde ligand [44]. Based on this, the lower energy mode at ∼640 cm^{-1} is assigned to the out-of-plane CH_2 wag in the complex, and the higher energy mode at ∼1240 cm^{-1}, to the C–O stretch. These values are in very good agreement with the corresponding vibrational mode frequencies for isolated formaldehyde in the π* state (683 and 1167 cm^{-1}, respectively) [44]. Note that these results are very different from the corresponding ground state frequencies due to the dramatic change in bonding in the excited state. (A comment on symmetry is warranted; initial excitation is to a state of B_2 symmetry in C_{2v} geometry, which is A'' with respect to the initial plane of the molecule [17]. After excitation the complex bends out-of-plane to form a C_s complex with the excited state being A' with respect to the new symmetry plane. To avoid confusion the symmetries here are consistently referred to the original plane of the molecule in the ground state.) The vibrational resonances in this band exhibit significant homogeneous linewidths, consistent with an upper state lifetime of <500 fs (or <7 vibrations of the Mg–O stretch, the mode that couples to the dissociation coordinate) [17]. Vibrational predissociation to an excited state asymptote is not energetically possible and dissociation requires coupling to the ground state surface through internal conversion.

The $3p_y\pi(A') \leftarrow 3s\sigma(A')$ band of $Mg^+(CH_2O)$ is expanded in Fig. 3a. There is an obvious short, anharmonic vibrational progression built on the band origin, with a fundamental frequency that corresponds to an intermolecular bending mode. Analysis of the partially resolved rotational substructure assigns the mode to the in-plane intermolecular bending vibration [17]. The observed rotational structure verifies the UCIS/6-311++g(2d,2p) predicted change in geometry to a bent complex with $\angle(\text{Mg–O–C}) = 139 \pm 3^\circ$ in the excited state. Additional progressions corresponding to combination modes with the intermolecular stretch are also easily identified. The vibrational mode frequencies for both the in-plane bend and intermolecular stretch modes are in excellent agreement with the UCIS model predictions. Birge–Sponer analysis of the short stretch progression in Mg^+-formaldehyde yields an excited state dissociation energy $D_e''(\text{Mg–OCH}_2) = 2.05$ eV, and through an energy cycle, an estimate for the bond energy in the ground state of $D_e''(\text{Mg–OCH}_2) = 1.21 \pm 0.2$ eV, which is somewhat lower than the UB3LYP/6-311++g(2d,2p) value of 1.45 eV. This agreement is reasonable given the experimental error and uncer-

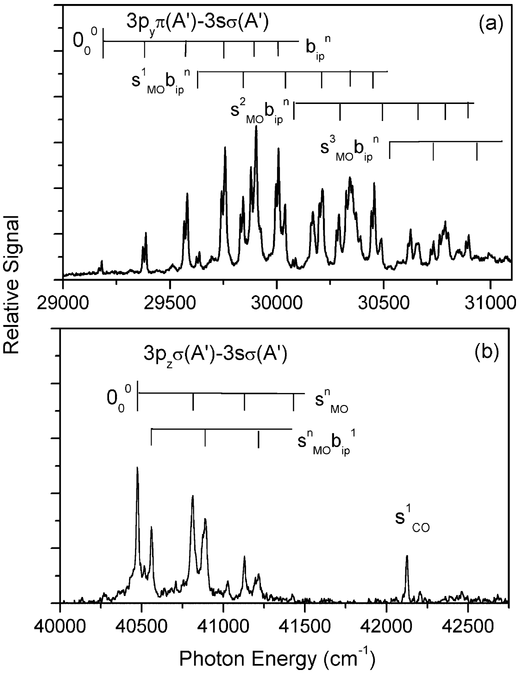

Fig. 3. Expanded views of the vibronic structure in the Mg^+-based $3p_y\pi(A') \leftarrow 3s\sigma(A')$ (a) and $3p_z\sigma(A') \leftarrow 3s\sigma(A')$ (b) bands of $Mg^+(CH_2O)$. The major features associated with the intermolecular Mg–O stretch (s_{MO}) and Mg–O–C in-plane bend (b_{ip}), and intramolecular C–O stretch (s_{CO}) modes are shown.

tainty in the Birge–Sponer extrapolation. It is interesting that the bending vibrational progression in Mg^+-formaldehyde shows an abrupt terminus at an energy ~900 cm^{-1} above the origin. This energy limit must correspond to a barrier to internal motion or isomerization, possibly a barrier corresponding to the transition state to the insertion complex [17].

An expanded view of the highest energy Mg^+-based $3p_z\pi(A') \leftarrow 3s\sigma(A')$ band of $Mg^+(CH_2O)$ is shown in Fig. 3b. There are short, low frequency vibrational mode progressions that correspond to combinations of intermolecular bending and stretching motions. Ab initio calculations show that electronic excitation in this band leads to a decrease in the Mg–O bond length as a partial Mg–O σ-bond forms, so that the Mg–O stretch mode should be active, consistent with the experimental spectrum. The experimental mode frequencies are in excellent agreement with the UCIS calculations for this state [17]. At much higher energy a vibrational resonance is observed that can be assigned to the intramolecular carbonyl C–O stretch mode, which is expected since the formation of a partial Mg–O bond will cause the C–O bond to weaken and stretch. There is no evidence for any other aldehyde intramolecular rocking or wagging motions that might be expected if the complex were to significantly distort away the planar geometry.

3.1.4. *Quenching dynamics*

These "half-collision" spectroscopic results suggest the dynamical pathways for the quenching of $Mg^{+}*(3p)$ in low energy, orbitally aligned O-end-on collisions with simple carbonyls. Such a process represents a useful model for developing a complete understanding of nonadiabatic processes in the chemistry of open shell systems. In Mg^+ $3p_x\pi(A'')$ approach symmetry the Mg^+ p_x-orbital is aligned perpendicular to the molecular symmetry plane and can effectively overlap the aldehyde π*-LUMO, allowing for efficient transfer of electron density into the carbonyl antibonding orbital that weakens and stretches the C–O bond. In Mg^+-formaldehyde the orbitals have comparable energies and the interaction is strong. Electron density can also be transferred from the oxygen lone pair nonbonding orbital into the empty Mg^+ s-shell. Quenching occurs primarily by vibronic coupling (*E–E*, V energy transfer) and results in $Mg^+(3s)$ and vibrationally hot aldehyde products.

For $Mg^{+}*(3p)$ approach in $3p_y\pi(A')$ symmetry the quenching will be less efficient and probably occur primarily through weak coupling to the lower (A'') energy surface, followed by *E–E*, V energy transfer quenching as described above. However, this physical quenching process may also compete with reactive quenching through C–H bond activation as noted below.

In Mg^+ $3p_z\sigma$ ($^2A'$) approach symmetry the Mg^+ p_z-orbital is aligned parallel to the Mg–O intermolecular axis and the geometry facilitates formation of a partial Mg–O bond, with a corresponding weakening of the C–O bond. The intermediate complex is likely to be long-lived and quench through *E–V* energy transfer, or through a competing reaction channel involving a direct attack on the aldehydic C–H bond in Mg^+-formaldehyde.

In $Mg^+(CH_2O)$ reaction to $MgH^+ + CHO$ products is observed with a branching that increases rapidly with increasing photolysis energy above the energetic threshold of ~30,000 cm^{-1}, approaching a reactive quantum yield of ~1/3 in the Mg^+ $3p_z\sigma(A') \leftarrow 3s\sigma(A')$ band [17]. The experimental and theoretical results suggest that the primary reaction mechanism in $Mg^+(CH_2O)$ is through C–H bond insertion. Based on results from Mg^+-acetaldehyde (below) where aldehydic C–C bond breaking is clearly observed [19], it is reasonable to assume that an insertive reaction pathway is open for activation of the aldehydic C–H bond in both Mg^+-formaldehyde and Mg^+-acetaldehyde as well. In addition, electronic structure calculations for $Mg^+(CH_2O)$ find an energetically accessible reactive intermediate that corresponds to the insertion complex HMgCHO, supporting this pathway. Reaction can occur in A' symmetry through a bond-stretch insertion mechanism that has previously been invoked to explain C–H bond activation in simple alkanes [10,12]. The in-plane Mg^+ p-orbital can overlap the unoccupied C–H σ*-antibonding orbital and the resulting transfer of electron density leads to a weakening and stretching of the C–H bond, which facilitates bond breaking through a side-on insertive attack geometry. The reaction need not go through to the fully inserted HMgCHO intermediate but may proceed through a distorted triangular transition state [10]. Coupling of the $3p_y\pi(A')$ and $3p_z\sigma(A')$ states through the intermolecular bending vibration can allow reaction from both excited states of A' symmetry, though the energetics favor the higher lying $3p_z\sigma(A')$ state. The proposed aldehydic C–H bond insertion reaction pathway is supported by electronic structure calculations on $Mg^+(CH_3CHO)$ [45]. Those calculations also suggest that methyl C–H bond activation should be possible, but that channel was not observed in $Mg^+(CH_3CHO)$ photodissociation.

Some contribution from an abstractive MgHCHO reaction pathway cannot be entirely ruled out; results for the analogous Zn^+-formaldehyde complex discussed below suggest that an abstraction reaction, facilitated by charge transfer, might play some role in the chemistry [21]. However, the relatively high energy of the charge transfer surfaces in Mg^+-formaldehyde, and the absence of any obvious charge transfer products in the dissociation suggest this pathway to be less likely. In addition, no stable abstractive geometry Mg^+–HCHO was found in the calculations.

3.2. *Mg^+-acetaldehyde*

It is interesting to compare results for Mg^+-formaldehyde and Mg^+-acetaldehyde. Ab initio calculations for $Mg^+–OCHCH_3$ finds a C_s-ground state equilibrium geometry with a slightly bent Mg–O–C bond, $\angle(\text{Mg–O–C}) = 172^\circ$, an Mg^+–O equilibrium bond distance, $R_{\text{Mg–O}} = 1.97$ Å, and a slightly higher bond energy at the UHF/6-311++g(2d,2p) level, $D_e''(\text{Mg–OCHCH}_3) = 1.87\,\text{eV}$ [18]. This calculated bond energy is similar to that found in Mg^+-acetone [46]. The excited state structure for Mg^+-acetaldehyde in a UCIS/6-311++g(2d,2p) calculation is quite analogous to that found for Mg^+-formaldehyde. Given the likeness in structure and bonding, it is not surprising that the electronic band spectra for Mg^+-formaldehyde and Mg^+-acetaldehyde should be similar as seen in Fig. 2. The band positions and structures for the three higher energy bands are closely comparable, as expected, and the spectroscopic assignment and analysis is similar. However the lowest energy $3p_x\sigma(A') \leftarrow 3s\sigma(A')$ band appears quite different; it is much weaker and more limited in range in Mg^+-acetaldehyde, indeed barely discernable on the scale of Fig. 2, and shows no evidence for vibrational structure.

The molecular orbital interactions in Mg^+-acetaldehyde should be analogous, and lead to a vibrationally hot complex following $3p_x\pi(A'') \leftarrow 3s\sigma(A')$ excitation. However in $Mg^+(CH_3CHO)$ the vibrational mode density is much higher, and the Mg–O bond strength is larger. As a result the weaker signal in Mg^+-acetaldehyde can easily be rationalized: the available energy deposited into the Mg–O intermolecular stretch mode that couples to the dissociation coordinate is simply too low to result in efficient dissociation of the complex for photon energies $<\sim 26{,}000\,\text{cm}^{-1}$.

In Mg^+-acetaldehyde several weak reactive quenching channels are also observed at the highest energies probed [18,19]:

$$Mg^+(OCHCH_3) + h\nu \rightarrow MgH^+ + CH_3CO \quad (4)$$

$$Mg^+(OCHCH_3) + h\nu \rightarrow MgCH_3{}^+ + HCO \quad (5)$$

$$Mg^+(OCHCH_3) + h\nu \rightarrow MgCHO^+ + CH_3 \quad (6)$$

Channels (5) and (6) correspond to breaking the C–C bond. Aldehydic H–D isotope substitution experiments verify that reaction (4) corresponds to attack on the aldehyde C–H bond rather than one of the methyl C–H bonds. The relative branching into the product channels that correspond to C–C versus C–H bond cleavage are roughly estimated as ∼1:1 for h-aldehyde and ∼2:1 for d-aldehyde. While these estimates are somewhat uncertain owing to mass overlap effects, it is clear that the probabilities for C–H and C–C bond cleavage are roughly comparable. It is also interesting that no branching to MgO^+ or $MgCO^+$ products, which might arise from more complicated rearrangement reactions is observed, even though these product channels are lower in energy. This suggests a direct single step insertive reaction mechanism from the excited state surface of A' symmetry as suggested earlier for $Mg^+(CH_2O)$. The essential elements of the C–H bond activation mechanism have been verified by ab initio electronic structure calculations [45]. C–C bond breaking was also observed in photodissociation of the closely related carbonyl complex $Mg^+(CH_3COOH)$, following excitation in the Mg^+-based $4p_z\sigma(A') \leftarrow 4s\sigma(A')$ band, suggesting a similar alignment preference for this reaction pathway [22].

The observation of comparable yields for reaction products resulting from C–H and C–C bond cleavage is interesting. In acetaldehyde, the aldehydic C–C and C–H bonds are of comparable strength and, in end-on $Mg^+–OCHCH_3$ geometry, appear similarly susceptible to attack by the metal ion. Steric effects do not seem to significantly hinder C–C bond activation. Because of the lesser overlap between the sp^3-hybridized orbital on the methyl carbon and the sp^2-orbital on the carbonyl carbon, molecular orbital reorientation appears less constrained in acetaldehyde than in alkane hydrocarbons.

3.3. *Ca^+-formaldehyde*

The influence of metal ion electronic structure and energetics on the bonding interactions and chemical dynamics can be studied by comparing results for $Mg^+(3s)$, $Ca^+(4s)$, and $Zn^+(3d^{10}4s)$-formaldehyde complexes. Despite the similar electronic valence character, these metal ions often show dramatically different interactions with small hydrocarbons and organic derivatives [10–21]. Generally, Ca^+ is found to be less reactive and more weakly interacting in both ground and excited states than either Mg^+ or Zn^+. For example, in $M^+(CH_4)$ clusters, excited $Mg^+(3p)$ and $Zn^+(3d^{10}4p)$ react efficiently through a nonadiabatic C–H bond insertion reaction, leading predominantly to $MCH_3{}^+$ product [10,12]. In contrast, $Ca^+(4p)$ is long-lived and weakly interacting, quenching inefficiently through energy transfer (probably to the lower $Ca^+(3d)$ state) [11]. These differences are due to a combination of energetic effects (including relative orbital and ionization energies), size effects (Ca^+ is significantly larger than either Mg^+ or Zn^+), and the presence of low-lying 3d-based molecular excited states in Ca^+ that open additional nonreactive quenching pathways.

$Ca^+(CH_2O)$ shows a C_{2v} ground state equilibrium geometry similar to $Mg^+(CH_2O)$, though with a somewhat weaker and longer bond reflecting the larger size of the ground state s-orbital for Ca^+ [20]. Geometry optimization at the UB3LYP/6-311++g(2d,2p) level shows an intermolecular bond with $R(\text{Ca–O}) = 2.28$ Å, and a dissociation energy of $D_e''(\text{Ca–O}) = 1.30\,\text{eV}$. No other stable geometries were found on the ground state surface for the weakly bound $Ca^+(CH_2O)$ complex.

Since both 3d and 4p excited states are important it is necessary to use a relatively large basis set to give an accurate picture of the excited state structure. UCIS/6-311++(3df,3pd) calculations on Ca^+-formaldehyde find at least nine excited states in the visible and near-UV, resulting from both metal centered Ca^+(3d and 4p ← 4s) and formaldehyde-based $\pi^* \leftarrow n$ excitations [20]. Molecular orbital analysis shows appreciable 3d–4p orbital mixing in the Ca^+-based transitions. While the degree of mixing is probably not quantitatively correct at the UCIS level due to correlation errors, the qualitative effect of the 3d–4p orbital mixing is to significantly enhance the oscillator strengths for the 3d ← 4s based molecular bands. The detailed spectroscopy has been described previously. Here we present results only for the states that correlate with the Ca^+ 4p levels for comparison to the Mg^+- and Zn^+-based complexes.

Interactions in the excited Ca^+-based 4p states of $Ca^+(CH_2O)$ are similar to $Mg^+(CH_2O)$. Geometry optimization for $4p_x\pi(A')$ finds a stronger Ca–O bond and a weaker C–O bond in comparison to the ground state, though the chemical interactions are significantly weaker than in the corresponding state of $Mg^+(CH_2O)$. The dominant vibrational modes observed in this band are assigned to the C–O and Ca–O stretches (Fig. 4a). As with $Mg^+(CH_2O)$, the change in bonding results from coupling between the Ca $4p_x$ and formaldehyde π^*-orbitals in this state, which weakens the C–O bond and allows formation of a partial Ca–O π-bond. The molecular orbital interaction is much weaker in $Ca^+(H_2CO)$ owing to the larger and more diffuse nature of the Ca 4p-orbitals, which lessens the orbital overlap, and to a larger energy gap between the metal p_x- and formaldehyde π^*-orbital energies.

Ab initio calculations and detailed spectroscopic analysis of the observed rovibronic structure in the $Ca^+(CH_2O)$ $4p_y\pi(A') \leftarrow 4s\sigma(A')$ band show that the upper state is bent with a Ca–O–C bond angle ∠(Ca–O–C) = 147 ± 2° [20]. As in $Mg^+(CH_2O)$ the change in geometry limits steric repulsion between the in-plane Ca^+ p_y-orbital and the O-lone pair electrons of the n-orbital of CH_2O. Again, the observed spectroscopic constants are in very good agreement with ab initio predictions for this state.

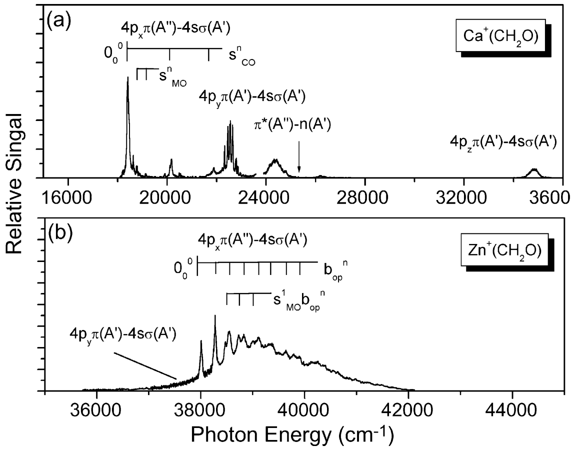

Fig. 4. Photodissociation action spectra for (a) $Ca^+(CH_2O)$ and (b) $Zn^+(CH_2O)$ with band assignments are shown. In $Zn^+(CH_2O)$ the Zn^+-based $4p_z\sigma(A') \leftarrow 4s\sigma(A')$ band is at much higher energies and is not observed. Vibrational features associated with the intermolecular M–O stretch (s_{MO}) and Zn–O–C out-of-plane bend (b_{op}), and intramolecular C–O stretch (s_{CO}) modes are shown. The vertical arrow in (a) marks the position of the Ca^+(4p ← 4s) atomic resonance line. The Zn^+(4p ← 4s) resonance line at 49,063 cm^{-1} is not shown.

The Ca^+-based $4p_z\sigma(A') \leftarrow 4s\sigma(A')$ band is significantly blue shifted from the Ca^+ 4p ← 4s atomic resonance, and appears as a continuum band with no vibrational resonance structure. An ab initio scan of the corresponding potential energy surface shows that the upper state is unbound, purely repulsive in the Ca–O coordinate. This is in contrast to Mg^+-formaldehyde where the analogous state is bound and shows partial Mg–O σ-bonding character.

Ca^+ is the only dissociation product observed from Ca^+-formaldehyde. Dissociation is possible through nonadiabatic coupling to the lower lying Ca^+ 3d-based excited states of the complex. The much weaker chemical interactions observed in Ca^+-formaldehyde are consistent with findings from other metal ion hydrocarbon complexes.

3.4. Zn^+-formaldehyde

3.4.1. Electronic structure calculations

Photodissociation spectroscopy of $Zn^+(CH_2O)$ shows results that are remarkably different from those for the analogous Mg^+- and Ca^+-based formaldehyde complexes. The differences are a result of the relatively high Zn ionization energy, which allow charge transfer (CT) interactions to play a dominant role in the chemical dynamics of this system. For comparison the ionization energies for Mg, Ca, and Zn are 7.64, 6.11, and 9.39 eV, respectively. Optimization calculations at the UHF/6-311++g(d,p) and MP2/6-311++g(d,p) (Moeller-Plesset 2nd order perturbation theory) levels find a ground state equilibrium for $Zn^+(H_2CO)$ with Zn bonded end-on to the O atom in a C_{2v}-association complex similar to previous results for the analogous Mg^+- and Ca^+-formaldehyde systems [21]. However, DFT calculations at the UB3LYP/6-311++g(d,p) level finds the most stable ground state complex to be bound in planar C_s symmetry with a Zn–O–C bond angle of ∠(ZnOC) = 140° (Fig. 1b). The calculated Zn–O equilibrium bond length is R(Zn–O) = 2.09 Å, with the formaldehyde ligand distorted only slightly from its isolated geometry. The calculated Zn–OCH_2 bond dissociation energy at the UB3LYP/6-311++g(d,p) level is D_e''(Zn–O) = 1.49 eV. These results differ qualitatively from the previous findings for Mg^+- and Ca^+-formaldehyde. The binding in $Zn^+(H_2CO)$ appears to be similar to $Cu^+(CH_2O)$ [47], with substantial CT character.

DFT calculations at the UB3LYP/6-311++g(d,p) level find two additional stable geometries on the ground state surface, which can be characterized as abstraction and insertion complexes as shown in Fig. 1b. The abstraction complex lies ~0.97 eV above the global minimum and has Zn^+ weakly bonded to the H-atom in a Zn^+-HCHO C_s geometry [21]. No analogous stable abstraction complex is found for Mg^+- or Ca^+-formaldehyde. A scan of the potential surface in the C–H bond coordinate shows there is no barrier for H-atom abstraction to ZnH^+ + CHO products above the reaction endoergicity. The

HZnCHO insertion complex in Fig. 1b lies 1.48 eV above the global minimum structure [21]. A similar, though more weakly bonded insertion complex was also found in Mg^+-formaldehyde (Fig. 1a).

Excited state calculations at the UCIS/6-311++g(d,p) level for Zn^+-formaldehyde find 3 strong Zn^+-based 4p ← 4s transitions and a weak formaldehyde-based $\pi^* \leftarrow n$ transition in the near UV, with character very similar to that found for the analogous transitions in Mg^+-formaldehyde [21]. However, because of the low ionization energy difference between Zn (IE = 9.394 eV) and CH_2O (IE = 10.88 eV), the charge transfer (CT) state in Zn^+-formaldehyde lies at very low energy and plays a major role in the spectroscopy and dynamics of this complex. The importance of the CT state is apparent from the observed product branching. Photodissociation of $Zn^+(CH_2O)$ in the near UV shows evidence for four major quenching channels (listed in order from lowest to highest energy) [21]:

$$Zn^+(CH_2O) + h\nu \rightarrow Zn^+ + CH_2O \tag{7}$$

$$Zn^+(CH_2O) + h\nu \rightarrow ZnH^+ + HCO \tag{8}$$

$$Zn^+(CH_2O) + h\nu \rightarrow Zn + CH_2O^+ \tag{9}$$

$$Zn^+(CH_2O) + h\nu \rightarrow ZnH + HCO^+ \tag{10}$$

The photodissociation product ion mass spectrum for $Zn^+(CH_2O)$ is shown in Fig. 5. The observed product branching is *opposite* to the energy ordering of these channels, so that HCO^+ is the most abundant and Zn^+ the smallest product. This is very different from the earlier results in Mg^+- and Ca^+-formaldehyde where nonreactive dissociation to the metal ion was the dominant quenching pathway.

A consideration of the potential energy surfaces can help clarify the discussion of the spectroscopy and dynamics of $Zn^+(CH_2O)$. Unfortunately, while the UCIS method can give very reliable results for the metal ion-based s–p transitions, UCIS results are often significantly in error for states with appreciable CT character. The asymptotic energy corrections are large for the CT state; the calculated $Zn + CH_2O^+$ asymptote lies at 4.80 eV, which is 3.31 eV above the value obtained from the experimental difference in ionization energies, $[IE(CH_2O) - IE(Zn)] = 1.49$ eV. This presents a problem for the analysis since the CT state obviously plays a pivotal role in the dissociation dynamics. However, experience has shown that UCIS level results can give valuable qualitative insight into the spectroscopy and dissociation dynamics if the calculated CT potential energy curves are simply shifted down to the correct asymptotic energy [15,21]. While this is obviously a crude approximation, more sophisticated time dependent DFT (TD-DFT) calculations of the CT state support the general conclusions drawn from this approach [21].

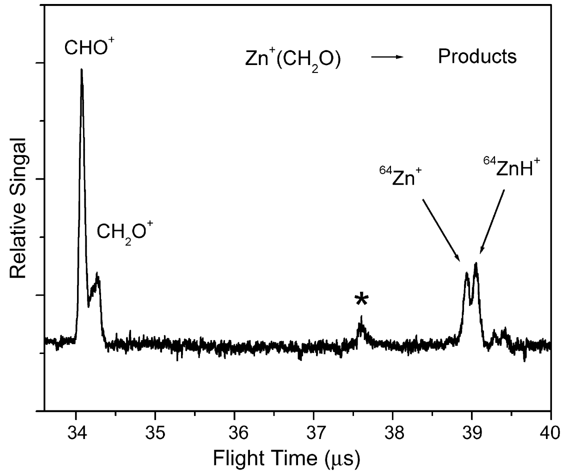

Fig. 5. Photofragment ion mass spectrum from the photodissociation of $Zn^+(CH_2O)$ at λ = 255 nm. Note the predominance of the charge transfer products. The peak labeled by * is an impurity from the source and is not a photodissociation product.

Fig. 6 shows two cuts through the ground and low-lying excited state potential energy surfaces for $Zn^+(CH_2O)$ calculated at the UCIS level. The charge transfer state, shown as the dashed line labeled 2A′, has been shifted down to the correct asymptotic energy as discussed. Fig. 6a shows the cut as a function of the Zn–C internuclear coordinate, while Fig. 6b shows a cut as the O–C–Zn angle increases from the global equilibrium value ∠(O–C–Zn) ~ 25° toward the Zn^+–HCHO abstraction interme-

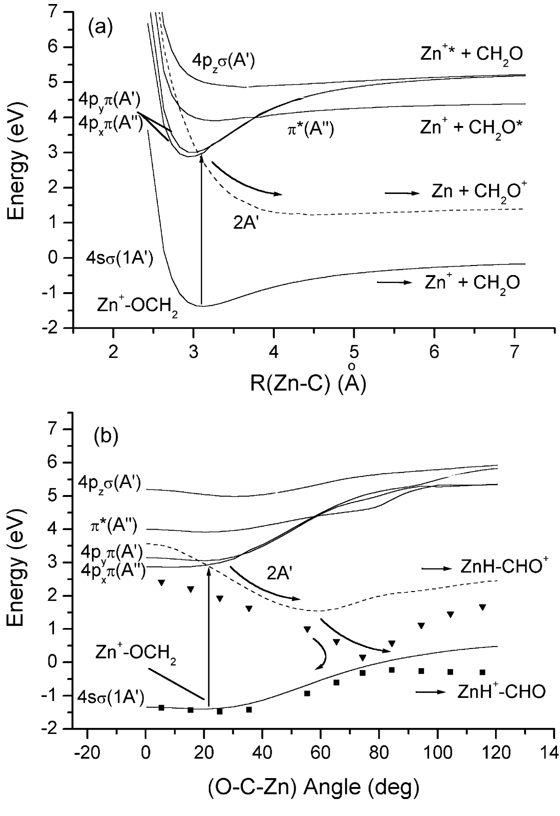

Fig. 6. Cuts through the low-lying doublet potential energy surfaces of $Zn^+(CH_2O)$, calculated at the UCIS/6-311++g(d,p) level: (a) cut as a function of Zn–C internuclear distance (with all other parameters held fixed at the global equilibrium values); (b) cut as a function of the O–C–Zn angle (with all other parameters held fixed at the global equilibrium values). The dashed curve labeled 2A′ corresponds to the charge transfer state that has been shifted down in energy by 3.31 eV from the UCIS result to match the correct asymptotic energy for charge transfer dissociation. The solid points in (b) correspond to TD-DFT/6-311++g(d,p) calculation results for the two lowest energy surfaces, the ground (squares) and charge transfer (triangles) surfaces. Arrows suggest competing dissociation pathways.

diate geometry with ∠(O–C–Zn) ~ 120°. The solid points in Fig. 6b show the two lowest states, $3s\sigma(1A')$ and the CT state $2A'$, recalculated at the TD-DFT/6-311++g(d,p) level. Differences with the shifted UCIS states are apparent, but qualitatively the results are in good agreement.

3.4.2. Electronic band spectra

The $Zn^+(CH_2O)$ photodissociation products all show similar action spectra as given in Fig. 4b. The spectra contain two overlapping absorption bands, a structured band superimposed on an underlying continuum. The underlying continuum band is assigned to a A' state in C_s symmetry, with an admixture of $Zn^+(4p_y\pi)$ and CT character. As expected from the potential energy surfaces, this state dissociates rapidly with the dominant branching to CT based products. This result, however, is very different from the behavior seen in the Mg^+- and Ca^+-based aldehyde complexes described above, where the analogous p_y state was relatively long-lived, and exhibited rovibrational structure consistent with a weakly interacting bent excited state. The vibrationally structured band in Zn^+-formaldehyde is assigned to the Zn^+-based $4p_x\pi$ $(^2A'')$ state, which is only weakly coupled to the CT surface.

3.4.3. Vibronic analysis

The $4p_x\pi$ $(^2A'') \leftarrow 4s\sigma(^2A')$ band shows at least two vibrational progressions built on the obvious origin near 38,000 cm^{-1}. The vibrational resonances show significant homogeneous broadening; the origin peak has a full-width at half-maximum (FWHM) ~45 cm^{-1}, consistent with an upper state lifetime of <~800 fs. There is an obvious long progression with a spacing of 277 cm^{-1}, assigned to the intermolecular out-of-plane wagging motion, and an additional short progression assigned to a combination mode with one quantum of the Zn–O intermolecular stretch mode [21]. The vibrational assignment in $4p_x\pi$ $(^2A'')$ indicates a distortion out-of-plane that is consistent with previous observations in both Mg^+- and Ca^+-formaldehyde and is expected through mixing with the $CH_2O(\pi^*)$ state (also A'').

3.4.4. Quenching dynamics

The experimental branching results can be understood with reference to the potential energy surface diagram in Fig. 6. Photoexcitation from the Zn^+–OCH_2 ground state equilibrium is to the overlapping Zn^+-based excited states $4p_x\pi(A'')$ and $4p_x\pi(A')$. Dissociation occurs primarily through coupling to the CT surface. Coupling from A'' to A' is indirect and can occur through a combination of rotational and vibronic interaction involving the out-of-plane wagging motion. The distribution of final product states is then determined by the dissociative branching on the CT surface ($2A'$), independent of the initially excited state.

On the $2A'$ CT surface the complex can dissociate directly, breaking the Zn–CH_2O bond and leading adiabatically to $Zn + CH_2O^+$ products (Fig. 6a). This is accompanied by significant kinetic energy release leading to an observable flight time broadening in the CH_2O^+ daughter (Fig. 5). Alternatively, the complex can bend in-plane on the $2A'$ CT surface toward the Zn–HCHO abstraction geometry, followed by an adiabatic reaction to $ZnH + CHO^+$ products with no barrier (Fig. 6b). The experimental results show this to be the primary dissociation pathway. The local forces and torques on the CT surface in the coupling region then determine the branching between major product channels, CHO^+ and CH_2O^+. The minor product channels, ZnH^+ and Zn^+ result primarily from nonadiabatic coupling back to the ground state surface in the bent complex, although some contribution from an insertion reaction in analogy with $Mg^+(CH_2O)$ may also be possible.

In the half-collision picture, quenching of $Zn^{*+}(4p)$ in a low energy collision with CH_2O proceeds primarily through long range CT, resulting in a competitive branching between "soft" CT quenching to $Zn + CH_2O^+$ products, and "hard" reactive quenching by H-atom abstraction to $ZnH + HCO^+$ products. Nonadiabatic quenching to the ground state surface through internal conversion is less efficient.

Photodissociation spectroscopy of Zn^+-formaldehyde complexes shows markedly different behavior from our previous observations in the Mg^+- and Ca^+-aldehyde clusters. These differences result primarily from the accessible low energy CT surface in the Zn^+-formaldehyde case that opens a direct adiabatic pathway to dissociation and reaction. In Mg^+- and Ca^+-aldehyde complexes the CT states are too high in energy to play any significant role in the chemical dynamics.

4. Summary

This review has focused on the spectroscopy and chemical dynamics of selected complexes of group II metal ions with simple aldehydes using mass resolved photodissociation spectroscopy techniques. The photodissociation spectroscopy of isolated metal ion-molecule complexes, coupled with results from electronic structure calculations of the low-lying potential energy surfaces, can help elucidate the underlying intermolecular interactions and chemical dynamics, and provide a rigorous test of the theoretical methods. The photochemical product action spectra yield information about the structure and lifetime of the complex, and the dynamical effects that determine the energy partitioning and microscopic branching in multichannel reactions. Such experiments give insight into the nuclear motion dynamics, stereochemical effects, and the electronic nonadiabatic interactions that couple the Born–Oppenheimer potential energy surfaces.

The metal ion-aldehyde complexes are generally bound in end-on M^+–OCRH geometry. The complexes show absorption bands in the visible and near UV that correlate with M^+-based, aldehyde-based, and CT-based radiative transitions. The spectroscopic character of the absorption bands, and the subsequent dissociation dynamics show wide variation depending on metal ion orbital alignment, size, and energetics. In Mg^+- and Ca^+-formaldehyde the metal ion-based p_x-orbital effectively couples with the carbonyl-based π^*-antibonding orbital of the aldehyde. Excitation to this state results in fast nonreactive *E*–*V* quenching and a vibrationally hot aldehyde product. In contrast excitation in the M^+-based p_y-bands of Mg^+- and Ca^+-formaldehyde lead to low frequency intermolecular bending vibrational motions consistent with a change in geometry from a linear M–O–C

(C_{2v}) ground state to a bent (C_s) excited state. Bending minimizes the overlap between the M^+ p_y-orbital and the O-based n-orbital of the carbonyl. Chemical interactions are relatively weaker in Ca^+-formaldehyde as a result of the larger more diffuse nature of the Ca^+ orbitals and larger energy gap between interacting orbitals. In the Mg^+-aldehydes reactive quenching is observed, and the evidence suggests that reaction occurs primarily through an aldehydic C–H and (in acetaldehyde) C–C bond insertion mechanism in A′ symmetry.

Photodissociation spectroscopy of Zn^+-formaldehyde demonstrates remarkably different behavior. These differences result primarily from the relatively high ionization energy of Zn that leads to a low energy CT surfaces in Zn^+-formaldehyde that opens new pathways for dissociation and reaction. In $Zn^+(CH_2O)$ CT facilitated reactive quenching dominates the dissociation.

Acknowledgments

This material is based upon work supported in part by the National Science Foundation under Grant CHE-9982119. Any opinions, findings, and conclusions or recommendations expressed in this material are those of the authors and do not necessarily reflect the view of the National Science Foundation.

References

[1] T. Hayes, D. Bellert, T. Buthelezi, P.J. Brucat, Chem. Phys. Lett. 264 (1997) 220;
D. Bellert, T. Buthelezi, P.J. Brucat, Chem. Phys. Lett. 290 (1998) 316.
[2] M.A. Duncan, Ann. Rev. Phys. Chem. 48 (1997) 69;
M.A. Duncan, Int. J. Mass Spec. 200 (2000) 545;
N.R. Walker, R.S. Walters, M.A. Duncan, New J. Chem. 29 (2005) 1495.
[3] J.M. Farrar, Int. Rev. Phys. Chem. 22 (2003) 593.
[4] D. Kim, S. Hu, P. Rarakeshwar, K.S. Kim, J.M. Lisy, J. Phys. Chem. A 107 (2003) 1228;
T.D. Vaden, J.M. Lisy, J. Chem. Phys. 120 (2004) 721.
[5] R.B. Metz, Int. Rev. Phys. Chem. 23 (2004) 79;
R.B. Metz, Int. J. Mass Spec. 235 (2002) 131.
[6] A. Furuya, J. Tsunoyama, F. Misaizu, K. Ohno, Chem. Phys. Lett. 382 (2003) 283.
[7] K. Ohashi, K. Terbaru, Y. Inokuchi, Y. Mune, H. Machinaga, N. Nishi, H. Sekiya, Chem. Phys. Lett. 393 (2004) 264.
[8] X. Yang, Y.H. Hu, S.H. Yang, J. Phys. Chem. A 104 (2000) 8496;
W.Y. Guo, H.C. Liu, S.H. Yang, Int. J. Mass Spec. 226 (2003) 291;
Y.H. Hu, R. Chen, L. Chen, X.J. Wang, H.C. Liu, S.H. Yang, Chem. Phys. Lett. 430 (2006) 255.
[9] P.D. Kleiber, J. Chen, Int. Rev. Phys. Chem. 17 (1998) 1.
[10] Y.C. Cheng, J. Chen, L.N. Ding, P.D. Kleiber, T.H. Wong, D.K. Liu, J. Chem. Phys. 104 (1996) 6452.
[11] J. Chen, Y.C. Cheng, P.D. Kleiber, J. Chem. Phys. 106 (1997) 3884.
[12] W.Y. Lu, T.H. Wong, P.D. Kleiber, Chem. Phys. Lett. 347 (2001) 183.
[13] J. Chen, T.H. Wong, K. Montgomery, Y.C. Cheng, P.D. Kleiber, J. Chem. Phys. 108 (1998) 2285.
[14] J.H. Holmes, P.D. Kleiber, D.A. Olsgaard, K.H. Yang, J. Chem. Phys. 112 (2000) 6583.
[15] W.Y. Lu, P.D. Kleiber, M.A. Young, K.H. Yang, J. Chem. Phys. 115 (2001) 5823.
[16] W.Y. Lu, R. Liu, T.H. Wong, P.D. Kleiber, J. Phys. Chem. A 106 (2002) 725.
[17] W.Y. Lu, T.H. Wong, Y. Sheng, P.D. Kleiber, J. Chem. Phys. 117 (2002) 6970;
W.Y. Lu, T.H. Wong, Y. Sheng, P.D. Kleiber, J. Chem. Phys. 118 (2003) 5267.
[18] W.Y. Lu, P.D. Kleiber, J. Chem. Phys. 114 (2001) 10288.
[19] W.Y. Lu, P.D. Kleiber, Chem. Phys. Lett. 338 (2001) 291.
[20] W.Y. Lu, T.H. Wong, Y. Sheng, P.D. Kleiber, J. Chem. Phys. 118 (2003) 6905.
[21] W.Y. Lu, Y. Abate, T.H. Wong, P.D. Kleiber, J. Phys. Chem. A 108 (2004) 10661.
[22] Y. Abate, P.D. Kleiber, J. Chem. Phys. 125 (2006) Art. No. 184310.
[23] B.M. Trost, I. Fleming, S.L. Schrelber (Eds.), Comprehensive Organic Synthesis, Pergamon Press, Oxford, 1991.
[24] C. Elschenbroich, A. Slazer, Organometallic Chemistry, Teubner, Stuttgart, Germany, 1994.
[25] J.J.R. Frausto da Silva, R.J.P. Williams, The Biological Chemistry of the Elements, Clarendon Press, Oxford University Press, Oxford, 1994.
[26] R. Atkinson, D.L. Baulch, R.A. Cox, R.F. Hampson, J. Kerr, J. Troe, J. Phys. Chem. Ref. Data 21 (1992) 1125.
[27] C.B. Moore, J.C. Weisshaar, Ann. Rev. Phys. Chem. 34 (1983) 525.
[28] R.B. Klemm, J. Chem. Phys. 71 (1979) 1987;
R.B. Klemm, E.G. Skolnik, J.V. Michael, J. Chem. Phys. 72 (1980) 1256.
[29] M. Dupuis, W.A. Lester, J. Chem. Phys. 81 (1984) 847;
M. Dupuis, W.A. Lester, J. Chem. Phys. 80 (1984) 4193.
[30] R.A. Ferrieri, A.P. Wolf, J. Phys. Chem. 96 (1992) 7164.
[31] C. Oehlers, H.G. Wagner, H. Ziemer, F. Temps, S. Dobe, J. Phys. Chem. A 104 (2000) 10500.
[32] H. Stauffer, R.Z. Hinrichs, J.J. Schroden, H. Floyd-Davis, J. Chem. Phys. 111 (1999) 10758.
[33] C.A. Bayse, J. Phys. Chem. A 106 (2002) 4226.
[34] J.J. Schroden, M. Teo, H. Floyd-Davis, J. Chem. Phys. 117 (2002) 9258.
[35] D.M. Sonnnenfroh, J.M. Farrar, J. Am. Chem. Soc. 108 (1986) 3521.
[36] L.M. Zhao, R. Zhang, W.Y. Guo, X.Q. Lu, Chem. Phys. Lett. 431 (2006) 56.
[37] P.A.M. Van Koppen, M.T. Bowers, C.L. Haynes, P.B. Armentrout, J. Am. Chem. Soc. 120 (1998) 5704.
[38] R.Z. Hinrichs, J.J. Schroden, H. Floyd-Davis, J. Phys. Chem. A 107 (2003) 9284.
[39] J.J. Low, W.A. Goddard, J. Am. Chem. Soc. 106 (1998) 8321.
[40] D.S. Cornett, S. Peschke, K. Laihing, P.Y. Cheng, K.F. Willey, M.A. Duncan, Rev. Sci. Instr. 63 (1992) 2177.
[41] T.G. Dietz, M.A. Duncan, M.A. Powers, R.E. Smalley, J. Chem. Phys. 74 (1981) 6511.
[42] W.C. Wiley, I.H. McLaren, Rev. Sci. Instr. 26 (1955) 1150.
[43] Gaussian 98, Revision A.6, M.J. Frisch, G.W. Trucks, H.B. Schlegel, G.E. Scuseria, M.A. Robb, J.R. Cheeseman, V.G. Zakrzewski, J.A. Montgomery, Jr., R.E. Stratmann, J.C. Burant, S. Dapprich, J.M. Millam, A.D. Daniels, K.N. Kudin, M.C. Strain, O. Farkas, J. Tomasi, V. Barone, M. Cossi, R. Cammi, B. Mennucci, C. Pomelli, C. Adamo, S. Clifford, J. Ochterski, G.A. Petersson, P.Y. Ayala, Q. Cui, K. Morokuma, D.K. Malick, A.D. Rabuck, K. Raghavachari, J.B. Foresman, J. Cioslowski, J.V. Ortiz, B.B. Stefanov, G. Liu, A. Liashenko, P. Piskorz, I. Komaromi, R. Gomperts, R.L. Martin, D.J. Fox, T. Keith, M.A. Al-Laham, C.Y. Peng, A. Nanayakkara, C. Gonzalez, M. Challacombe, P.M.W. Gill, B. Johnson, W. Chen, M.W. Wong, J.L. Andres, C. Gonzalez, M. Head-Gordon, E.S. Replogle, J.A. Pople, Gaussian, Inc., Pittsburgh PA, 1998.
[44] D.C. Moule, A.D. Walsh, Chem. Rev. 75 (1975) 67.
[45] W.Y. Guo, T. Yuan, X.F. Chen, L.M. Zhao, X.Q. Lu, S.J. Wu, J. Molec. Struc. Theochem. 764 (2006) 177.
[46] J. Velasquez, E.D. Pillai, P.D. Carnegie, M.A. Duncan, J. Phys. Chem. A 110 (2006) 2325.
[47] S. Hoyau, G. Ohanessian, Chem. Phys. Lett. 280 (1997) 266.